Research Article Vol. 5, No. 6 / June 2018 / Optica 695

Thermodynamic control of soliton dynamics in liquid-core fibers

Mario Chemnitz,[1,*] Ramona Scheibinger,[1] Christian Gaida,[2] Martin Gebhardt,[2,3] Fabian Stutzki,[2,4] Sebastian Pumpe,[5] Jens Kobelke,[1] Andreas Tünnermann,[2,3,4] Jens Limpert,[2,3,4] and Markus A. Schmidt[1,6]

[1]Leibniz Institute of Photonic Technology, Abbe Center of Photonics, Albert-Einstein-Str. 9, 07745 Jena, Germany
[2]Institute of Applied Physics, Abbe Center of Photonics, Friedrich-Schiller-University Jena, Albert-Einstein-Str. 15, 07745 Jena, Germany
[3]Helmholtz-Institute Jena, Froebelstieg 3, 07743 Jena, Germany
[4]Fraunhofer Institute for Applied Optics and Precision Engineering, Albert-Einstein-Str. 7, 07745 Jena, Germany
[5]Deutsches Elektronen-Synchrotron (DESY), Notkestrasse 85, 22607 Hamburg, Germany
[6]Otto Schott Institute of Material Research, Abbe Center of Photonics, Friedrich Schiller University of Jena, Fraunhoferstrasse 6, 07743 Jena, Germany
*Corresponding author: mario.chemnitz@leibniz-ipht.de

Received 14 November 2017; revised 15 February 2018; accepted 28 February 2018 (Doc. ID 313448); published 29 May 2018

Liquid-core fibers offer local external control over pulse dispersion due to their strong thermodynamic response, offering a new degree of freedom in accurate soliton steering for reconfigurable nonlinear light generation. Here, we show how to accurately control soliton dynamics and supercontinuum generation in carbon disulfide/silica fibers by temperature and pressure tuning, monitored via the spectral location and the onset energy of non-solitonic radiation. Simulations and phase-matching calculations based on an extended thermodynamic dispersion model of carbon disulfide confirm the experimental results, which allows us to demonstrate the potential of temperature detuning of liquid-core fibers for octave spanning recompressible supercontinuum generation in the near-infrared.

OCIS codes: (060.4370) Nonlinear optics, fibers; (060.2390) Fiber optics, infrared; (190.4400) Nonlinear optics, materials; (190.5530) Pulse propagation and temporal solitons; (320.6629) Supercontinuum generation.

https://doi.org/10.1364/OPTICA.5.000695

1. INTRODUCTION

Fiber-based nonlinear light sources with tailored properties are used in a large number of applications, including nonlinear imaging [1], spectroscopy [2,3], optical metrology [4,5], and telecommunications [6,7], and rely mostly on crystalline or amorphous materials. Despite their great benefits, the use of solid materials imposes restrictions to the external control of nonlinear output signals. Besides detuning the pump [8,9] or using additional seed sources, direct tuning of nonlinear processes is difficult due to the limited gain bandwidth of the driver laser or an overall restricted nonlinear gain [10].

One straightforward tuning scheme for external control of optical properties relies on changing the ambient temperature of the respective device (e.g., used for measuring high temperatures [11] or for tuning into Kerr soliton states in microresonators [12]). Within fiber optics, however, the thermo-optic coefficients of most glasses and, in particular, that of silica glasses are rather low (e.g., 8.6×10^{-6} K^{-1} for fused silica [13]), and the impact of temperature on modal properties is limited. Another promising solution are gas-filled hollow-core fibers, allowing wide tuning of UV light generation [14], with the expense of requiring high pulse energy and highly specialized fiber designs.

In addition to broad transmission windows [15] and large nonlinearities [16], liquid-filled fibers promise great potential for external control over linear as well as nonlinear optical properties due to miscibility and strong thermodynamic effects. In particular, the large thermo-optical response of liquid-infiltrated fibers suggests strong impact on the optical properties, which can be used for temperature sensing [17,18], wavelength detuning of microfluidic lasers both on-chip [19,20] and potentially in-fiber [21], spatial mode coupling [22,23], spectral filtering [24,25], and for nonlinear signal detuning [26]. However, the full tuning potential of liquids for advanced nonlinear applications (e.g., supercontinuum generation) can only be uncovered if the underlying thermodynamic dispersion model is known, which still remains unclear for all liquids commonly used in optics. To our knowledge all existing studies use a linear thermo-optic model [26–28], which is limited in predicting phase-matching over a broad bandwidth and especially in proximity to a strong absorption.

In this work, we use dispersive wave generation (DWG) (i.e., Cherenkov radiation or non-solitonic radiation), which is well known to be the initial part of complex soliton dynamics in supercontinuum generation [29] and to be highly sensitive to

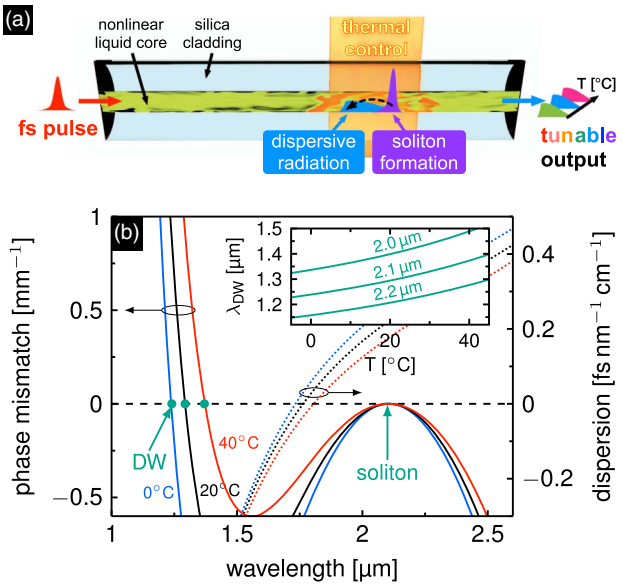

Fig. 1. Thermo-optic effect on DWG in liquid-core fiber. (a) Device principle: the thermodynamically modified mode dispersion influences the DW radiated off a solitary pump wave. (b) Group velocity dispersion (right axis) of a CS_2/silica step-index fiber with core diameter of 3.3 μm for three temperatures and the corresponding phase mismatch (left axis) between a DW and a hypothetical pump soliton at 2.1 μm in the same fiber. The inset shows the temperature dependence of the wavelength of perfectly phase-matched DWs for three different pump solitons at 2.0, 2.1, and 2.2 μm.

waveguide dispersion, to monitor the influence of thermodynamic changes on soliton fission in liquid-core optical fibers (LiCOFs) filled with carbon disulfide [scheme shown in Fig. 1(a)]. We correlate accurate measurements of the spectral location and onset energy of the first dispersive wave (DW) at different temperatures and pressures with simulations and phase-matching calculations to unveil the potential of LiCOFs with regard to external system control. Finally, we present a realistic concept for a highly coherent supercontinuum spanning two octaves of spectral bandwidth at moderate pump energies and pump wavelength of 1.55 μm using a longitudinal temperature-induced dispersion gradient.

2. DEVICE PRINCIPLE AND DESIGN

Thermodynamic tuning of the DWG process fundamentally relies on modifying the underlying phase-matching condition [30]:

$$\beta(\omega) - \beta(\omega_s) + (\omega_s - \omega)\beta_{1,s} - \gamma_s P_s/2 = 0, \quad (1)$$

with the propagation constant β (obtained from solving the transcendental dispersion equation of a cylindrical step-index fiber), the angular frequency ω of the linear (dispersive) wave, and the group velocity parameter $\beta_{1,s} = \partial\beta/\partial\omega|_{\omega_s}$, the nonlinear parameter γ_s, and the peak power $P_s = P_0 \cdot (2N - 1)^2/N^2$ [31] (with input peak power P_0 and soliton number N) of the assumed first solitary wave with angular frequency ω_s. The delayed nonlinear response of liquids contains a significant noninstantaneous nonlinear contribution, which, however, has a negligible effect on the phase-matching condition [32]. Hence, the nonlinear parameter $\gamma_s = \omega n_{2,el}/(cA_{eff})$ (with vacuum speed of light c and effective mode field area A_{eff}) and the soliton number N used in Eq. (1) contain only the electronic nonlinear refractive index (RI) $n_{2,el}$ [33].

Equation (1) clearly suggests that any change of the model dispersion has direct consequences on the wavelength of the generated DW, in particular since $\beta(\omega)$ includes a distinct frequency dependence. Thus, precise knowledge about the thermodynamic properties of the RI dispersion of the various media involved is required.

To date, thermo-optical (TOCs) and piezo-optical coefficients (POCs) of liquids have been mostly modeled as wavelength independent by imposing a constant value added to the respective RI at any wavelength. Thus, the impacts of temperature and pressure on nonlinear and, in particular, on phase-matching processes that demand including higher order derivatives of $\beta(\omega)$ (e.g., group velocity or group velocity dispersion) are neglected. The assumption of constant coefficients is in fact unphysical, since the bandwidth and positions of the electronic and molecular transitions (both depending on temperature and pressure) dictate material dispersion via the Kramers–Kronig relation. A spectral distribution of the TOC has only been determined for a few selected solvents [34–37], but the physical models assumed here do not justify an extension of the validity bandwidth beyond the visible.

Here we choose carbon disulfide (CS_2) as core material, since its optical properties (absorption, dispersion [32], and nonlinearity [33]) are reasonably well known compared to other liquids. Also, we recently measured its TOC and POC over an extended spectral domain from the visible to the starting near-infrared (near-IR) [38], by which we can construct a temperature-dependent RI dispersion model for CS_2 analogously to those used for glasses [39,40]. We (i) took the RI of CS_2 $n_0(\lambda_k)$ using a known Sellmeier model [32] at the wavelengths λ_k where the TOC is known, (ii) calculated new values of the RI for a selected temperature T_l using the linear thermo-optical relation $n(\lambda_k, T_l) = n_0(\lambda_k) + dn/dT|_{T_0}(\lambda_k) \cdot (T_l - T_0)$ (with $dn/dT|_{T_0}$ as TOC at room temperature $T_0 = 20$°C), and (iii) fitted the wavelength dependence of all $n(\lambda_k, T_l)$ with a new Sellmeier equation. This process is repeated for multiple temperatures T_l between 0°C and 40°C whereby each temperature yields a new set of Sellmeier coefficients ($B_{1,l}$, $C_{1,l}$). However, the TOC is not known beyond the near-IR, and, thus, we had to assume the second Sellmeier term (IR resonance) to be a constant, which is, however, in good approximation with the weaker impact on the total RI in the near-IR spectral domain, too (i.e., a smaller amplitude parameter than the UV term: $B_2 \ll B_1$). Finally, we approximated the temperature dependence of the two parameters $B_{1,l}$ and $C_{1,l}$ by polynomials. In the case of the POC, however, the measured data are too sparse to repeat the fitting process for the pressure influence. Thus, we use the common linear approximation to account for piezo-optic effects. The final expression for the pressure and temperature dependent RI dispersion of CS_2 yields the following thermodynamic Sellmeier equation:

$$n(\lambda, T) = \left(1 + \frac{B_1(T)\lambda^2}{\lambda^2 - C_1^2(T)} + \frac{B_2\lambda^2}{\lambda^2 - C_2^2}\right)^{1/2} + \left.\frac{\partial n}{\partial p}\right|_{p_0, T_0}(p - p_0), \quad (2)$$

where $dn/dp_{p_0, T_0} = 682 \times 10^{-12}$ Pa^{-1} is the POC at atmospheric pressure ($p_0 = 10^5$ Pa) and room temperature T_0 [41]. The resulting Sellmeier coefficients in Table 1 allow us to accurately describe the impact of temperature and pressure on the RI dispersion of CS_2 from UV to near-IR wavelengths.

Table 1. Sellmeier Coefficients of Carbon Disulfide[a]

B_1 (T [K])	$2.17144765 - 0.66589562(T/T_0)$
B_2	0.085924705
C_1 (T [K]) [μm]	$0.18382049 - 0.00505833(T/T_0)$ $-0.00421529(T/T_0)^2$
C_2 [μm]	6.48315928

[a]T: temperature in K, $T_0 = 293.15$ K.

With the precise knowledge of the RI dispersions of core and cladding (CS_2 from Eq. (2) and SiO_2 from [42]) we are able to predict the wavelength of the DW λ_{ZD} for a given soliton wavelength via Eq. (1) [example shown in Fig. 1(b)]. For instance, the wavelength at which the dispersion parameter ($D = -2\pi c/\lambda^2\beta_2$ with the group velocity dispersion $\beta_2 = \partial^2\beta/\partial\omega^2$) of the fundamental mode HE_{11} vanishes [i.e., the zero-dispersion wavelength (ZDW) λ_{ZD}] redshifts by 55 nm with a 40 K temperature increase. This causes a blueshift of the DW by a few hundreds of nanometers depending on the initial soliton wavelength and assuming a realistic temperature range between 0°C (water condensation limit) and 46°C (boiling point of CS_2) (see inset of Fig. 1). It is important to note that the TOC of silica is about two orders of magnitude smaller than that of CS_2 and is, thus, negligible for the experiments reported here.

Soliton-based DWG requires the waveguide to operate in the anomalous dispersion domain close to λ_{ZD}. By filling CS_2 ($\lambda_{ZD} = 2.4$ μm) into a fused silica capillary, we are able to shift λ_{ZD} of the HE_{11} mode below 1.9 μm at comparably large core diameters, allowing for reasonable coupling efficiencies. The strongest impact of temperature on λ_{ZD} and DWG is found for core diameters between 2.5 and 4 μm (dotted region in Fig. 2) in a region omitted by other studies to date. LiCOFs with core diameter larger than 6 μm show only a weak dependence on temperature, whereas the interplay of core and cladding dispersion is not as critical. For our experiments, we used a core diameter of 3.3 μm (available diameter closest to 3 μm), which

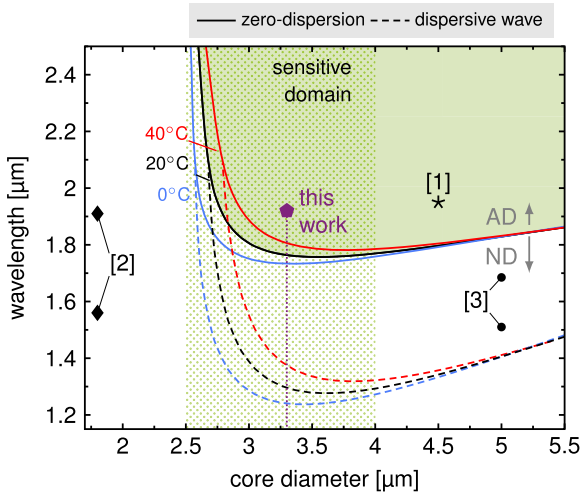

Fig. 2. ZDW of the fundamental mode (HE_{11}) and the phase-matching condition as function of the core diameter of a CS_2/silica step-index fiber for three temperatures. For the phase-matching calculation, a solitary wave at 2.1 μm was assumed. The marks highlight the pump wavelengths of former work in the field and our contribution, which is within the temperature-sensitive domain (dotted). The anomalous and normal dispersion domains are denoted as AD and ND.

enables us to optically pump the system in the highly temperature sensitive domain in the anomalous dispersion regime close to λ_{ZD} at 1.8 μm with thulium-doped fiber lasers.

3. EXPERIMENT

The supercontinuum generation (SCG) experiments were based on a setup that combines an ultrafast pulsed laser source operating at 1.92 μm wavelength with an optofluidic system (see Fig. 3). As the ultrafast pump source, we combined a customized thulium-doped fiber laser (25 MHz, 1.92 μm, 500 fs) with a dispersion-managed fiber amplifier, as reported earlier [43]. The initial seed pulses are pre-chirped and subsequently amplified based on a nonlinear amplification scheme, which leads to a slight compression. The output of the amplifier (350 fs FWHM pulse width) was monitored online with two 3% reflexes, coupled into an autocorrelator and a spectrometer (for details on the laser specifications see Supplement 1).

Efficient coupling into the CS_2-LiCOF was ensured by home-build optofluidic fiber mounts (OFMs) featuring two fluidic ports (inlet and outlet) and one central fiber port facing a sealed sapphire window, which enable simultaneously filling of CS_2 and light coupling into the liquid core. Flushing one OFM with CS_2 via a syringe initiates filling of the entire channel purely by capillary action. After 20–30 min, the ports of the first OFM are sealed with plugs, and the second OFM is flushed with CS_2 and sealed to ensure a defined output end face of the LiCOF. The dead volume in the holder is approximately 1 ml.

After preparation, the LiCOF (NA = 0.65, $V = 3.55$ at 1.9 μm, length 18 cm) was aligned in the optical setup between two coupling stages. Coupling efficiencies to the fundamental mode of about 25%–30% have been achieved, taking into account an absorption of about 26% along 18 cm of fiber length and the reflections at the various interfaces. The coupling and, in particular, the fundamental output mode were stable over days and during all experiments. As reported in earlier work [32], we did not directly observe bubble formation, but we observed mode instabilities and a drastic drop in the transmission efficiency as soon as we reached 150 mW average power. Spectral measurements were performed by using two optical spectral analyzers (OSA domains: 0.7–1.7 μm, 1.2–2.4 μm) and an InF_3 multimode fiber.

Since controlling the temperature along the entire fiber, including OFMs and coupling stages, homogeneously is practically difficult, a Peltier element (maximum power 72 W) placed at a well-selected section close to the fiber end enabled accurate temperature control between 0°C and 40°C over a length of 7 cm. The fiber was fixed with an aluminum plate on top of the Peltier element as close as possible to the OFM at the output side. The Peltier element itself was placed on an aluminum cooling body [see base plate in Fig. 3(d)]. Thermal conduction paste ensured efficient heat transfer among all mechanical parts.

Uncovering the impact of temperature on DWG as clearly as possible requires identifying an appropriate power level slightly above the soliton fission energy, which needs to be sufficiently low to avoid multiple DWG. Therefore, we measured the output spectra of the LiCOF for increasing input powers [see Fig. 3(a)] and compared the results with simulations [see Fig. 3(b)] based on solving the generalized nonlinear Schrödinger equation (GNLSE). The GNLSE used includes a full loss spectrum [32], modal dispersion, dispersive nonlinearity, and the full

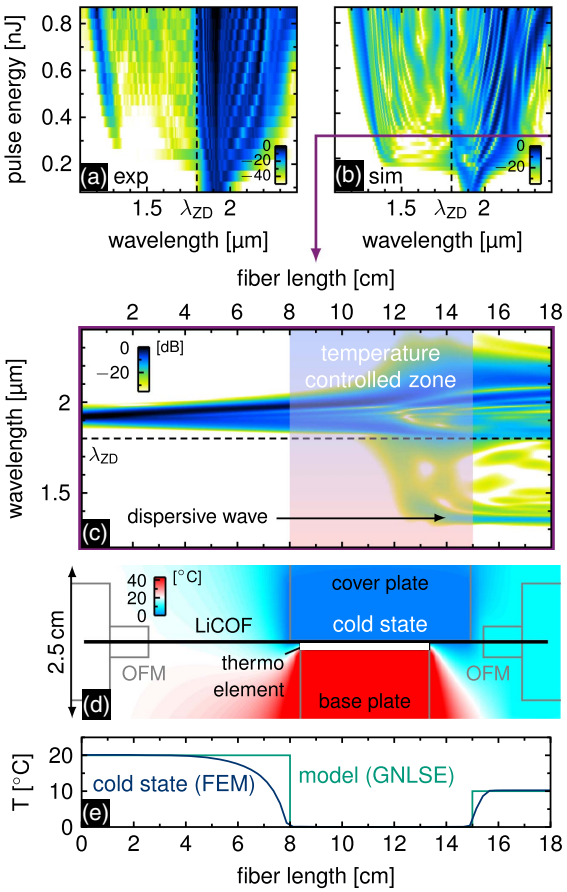

Fig. 3. Supercontinuum output and tuning configuration. (a) Measured output spectra of 18 cm CS_2/silica fiber for increasing initial in-fiber pulse energy. (b) Simulated output spectra of the same fiber in the same pump energy domain using a reconstructed pulse shape. (c) One individual spectral evolution of a 350 fs pulse with 0.3 nJ pulse energy. The blue–red zone highlights the soliton fission area where a temperature element has highest impact. (d) Heat map of the liquid-core fiber placed on a 5 cm heating element. (e) Temperature profile along the fiber core in the cold state (calculated) compared to the temperature distribution assumed in our simulations (GNLSE).

nonlinear response of CS_2 [33] (see Supplement 1). The optical pulse used in the simulation is the transform limit of the measured spectrum (full width at half-maximum 150 fs sech^2) chirped up to 350 fs with a positive group delay dispersion of $D_2 = 1.7 \times 10^4$ fs^2 to match the measured autocorrelation width (see Supplement 1). Experiment and simulation match well in terms of soliton fission energy, generated bandwidth, and visible spectral features (e.g., the spectral location of the DW and spectral modulations at wavelengths >1.9 μm). Small deviations (e.g., in the residual pump power and the contrast on the DW side) might originate from a simplified loss model in the simulation, deviations in pulse shape and chirp or chromatic aberrations on the diagnostics side. In accordance with our previous findings [32], we observe soliton fission instead of modulation instabilities, which become particularly dominant in glass fibers at relatively long pulses (i.e., 350 fs) and large soliton numbers (here $N \approx 20$).

At pulse energies around 0.3 nJ, an isolated spectral signal around 1.3 μm is visible in the experiment [see Fig. 3(a)], which is associated with a single DW generated toward the end of the fiber according to the simulated evolution of the pulse spectrum along the fiber in Fig. 3(c). The simulation confirms that the temperature influence on the initial DWG process can be made visible solely by heating or cooling the last section of the LiCOF. Moreover, the calculated two-dimensional temperature distribution (COMSOL Multiphysics) of the configuration finally used in the experiment [shown in Fig. 3(d)] promises a constant temperature along the locations the DW is generated, in particular along the length of the active cooling region [see Fig. 3(e)]. Note that already the dispersion landscape induced by such a simple temperature treatment requires careful tapering in the case of glass fibers, whereas the resulting dispersion profile is static. Moreover, in the present situation, the relative change of the dispersion can even be flipped in sign, i.e., the change of dispersion correlating with heating is opposite to the case of cooling—an operation which is exceedingly hard to achieve using tapering. In practice, also note that the OFM at the output side acts as a heat cavity and hinders the temperature at the fiber output to return to room temperature. In our model, the final temperature turned out to be approximately half of the temperature of the thermoelement.

4. TEMPERATURE DETUNING OF NON-SOLITONIC RADIATION

We implemented the configuration as shown in Fig. 3(d) and measured the power/spectral evolution of the supercontinuum process at low (2°C) and high (36°C) temperature of the thermoelement shown in Figs. 4(a) and 4(b). Compared to the cold state, the high-temperature configuration reveals a drastic decrease in onset energy from 360 to 240 pJ (±20 pJ) and a redshift of the spectral location of the initial DW. The difference can be primarily explained by the temperature-modified dispersion landscape of the LiCOF: in the cold state, the dispersion

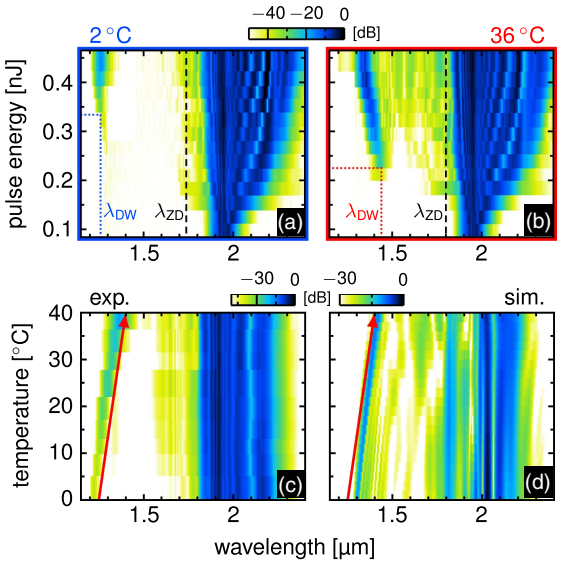

Fig. 4. Impact of temperature on DWG. (a) and (b) Measured output spectra of the CS_2/silica fiber for increasing input pulse energy in the (a) cold and (b) hot state of a 5 cm Peltier element placed close to the fiber end. (c) and (d) Measured and simulated output spectra compared for constant input pulse energy of 0.25 nJ and increasing temperature. The arrow is placed at the same position and with the same orientation in both figures for a better comparison.

parameter is increased and the ZDW λ_{ZD} is located at a shorter wavelength compared to the high-temperature situation. Thus, the phase-matching wavelength λ_{DW} of the DW lies more distant from the pump wavelength, and the initial pulse needs stronger nonlinear compression to gain the necessary spectral overlap to seed the distant DW. The necessary compression, even though accelerated by the higher dispersion parameter at the pump wavelength, requires higher pulse energies, which explains the higher fission energy in the cold state. In the hot state, the conditions are exactly reversed: λ_{ZD} and λ_{DW} are closer to the pump wavelength, thus less compression and less fission energy is required. The impact of temperature on the soliton side is less obvious in the power/spectral evolutions and cannot be deduced from measurements only.

To understand the behavior of the DW more accurately, we recorded the output spectrum for increasing temperature at a constant in-fiber pulse energy of 0.25 nJ. Even though the spectral location of the DW reacted immediately to a temperature change, we waited several minutes to ensure that the system reached thermal equilibrium before recording the individual spectra. The measurements in Fig. 4(c) reveal a quasi-linear redshift of the DW of about 140 nm over a 40 K temperature domain, corresponding to a shift of 3.5 nm/K. Furthermore, we observe a continuous increase of the spectral intensity and the bandwidth of the DW with increasing temperature. The spectral location of the corresponding initial soliton, however, stays nearly constant at around 2.15 μm.

We modeled the modified soliton fission process by extending our GNLSE solver such that it handles successive fiber sections of temperature-modified modal dispersions. We approximated the temperature profile by three fiber sections at constant temperature [see Fig. 3(e)], and the nonlinear parameter was recalculated each few hundred steps to account for the noninstantaneous nonlinear contribution to the nonlinear RI of CS_2. This is necessary since the rise and decay times of the nonlinear response of CS_2 are of the order of the pulse width, leading to an effective nonlinear RI changing with the evolving pulse [33]. This effect is not fully covered by the convolution term of the GNLSE in the standard definition as outlined in Supplement 1. The simulated output spectra in Fig. 4(d) qualitatively resemble the measured behavior of the DW and the corresponding soliton for all temperatures. Figure 5 shows the measured and simulated spectral locations of the intensity maximum of the initial DW and soliton at each temperature quantitatively. First, we note that the initial solitary wave remains at the same wavelength in both experiment and simulation within the applied temperature range. The measured and simulated DWs, although located at slightly different absolute wavelengths, show almost identical relative redshifts from −5% to +5% when increasing temperature. In addition to the model assumptions mentioned previously, the small deviations might arise from the assumed temperature profile, particularly the assumed constant temperature of the last 3 cm of propagation, which turned out to significantly impact the DW location after fission.

As a further benchmark, we calculate the DW location using the phase-matching condition in Eq. (1) assuming that the first soliton is located at around 2.1 μm with peak power $P_s = 2.9$ kW (and $\gamma_s = 62$ W^{-1} km^{-1}) at any of the temperatures considered. The obtained phase-matched wavelengths (dashed green lines in Fig. 5) match the measured DW locations and thus

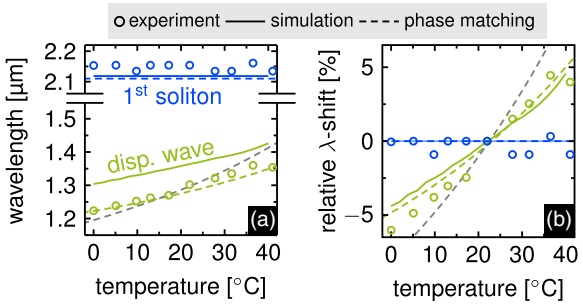

Fig. 5. Temperature dependence on (a) the absolute wavelength and (b) relative wavelength shift of the first (most long-wave) soliton and the strongest DW as measured, simulated, and calculated from the phase-matching condition. The gray dashed lines show the DW wavelength in the case of perfect phase matching using a linear TOC model as a comparison to our model (green dashed lines) from Eq. (2).

resemble the redshift very well. The small constant offset between the measured and assumed soliton wavelengths is most probably caused by the neglect of the nonlinear phase and the soliton recoil effect [44]. In contrast, we calculate the phase-matching wavelength using the linear (non-dispersive) TOC model (dashed gray lines in Fig. 5), which highlights that this coarse assumption results in an overestimation of the bandwidth of the shift.

5. PRESSURE DETUNING OF FISSION ONSET

In addition to the paradigm of the incompressibility of liquids, pressure (i.e., density or viscosity modification) has a measurable impact on the dispersive and potentially the nonlinear properties of a liquid-core fiber [16,34], and, thus, on the SCG process. As a proof-of-concept, we applied a static pressure to the fluidic inlets of both OFMs with a high-pressure pump, whereas the outlets were blocked with high-pressure valves. We measured the output spectra around the DW onset energy for atmospheric pressure [see Fig. 6(a)] and a pressure of 100 bar [see Fig. 6(b)]. The coupling efficiencies have been carefully controlled to provide identical coupling conditions. Note that these experiments rely on a different CS_2-LiCOF configuration (core diameter 4.6 μm,

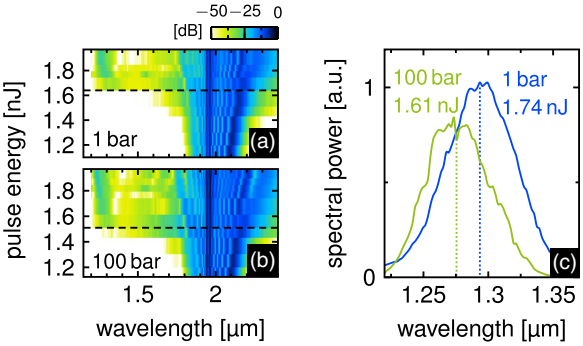

Fig. 6. Measured output spectra as functions of input pulse energy for two different applied pressures: (a) atmospheric pressure (1 bar) and (b) 100 bar. The dashed horizontal lines indicate the onset pulse energy of the DWG (i.e., the fission energy). (c) Spectral intensity profile of the initial DW at the two pressure states. The spectra have been selected accordingly to the pulse energy at which the DW is clearly distinguishable from the solitary background for the first time. The dotted lines mark the positions of the non-solitonic radiation at the onset.

length 8 cm) and a different thulium fiber laser system with 450 fs output pulses both reported in [32]. Thus, the onset energies vary compared to the previous fiber. Because of the larger core diameter, thermodynamic effects influence the mode dispersion less, as shown in Fig. 2.

Under atmospheric pressure we measured the DW onset at 1.64 nJ (±0.03 nJ) energy and 1.3 μm wavelength, whereas at 100 bar the onset energy reduced to 1.51 nJ (±0.03 nJ) with λ_{DW} remaining at around 1.3 μm. The calculated ZDW based on our model in Eq. (2) reveals only a slight pressure-induced blueshift of about 10 nm, which is presumably the reason for the slight blueshift of the measured DWs of about 20 nm [see Fig. 6(c); each measured at the lowest energies at which the individual DW is still distinctly visible].

The change of the fission energy can be understood from the estimation of the fission length introduced by Dudley *et al.* [31]:

$$L_{\text{fiss}} \approx L_{\text{D}}/N \propto (E_{p,\text{fiss}}|\beta_2|)^{-\frac{1}{2}}, \tag{3}$$

where L_{D} is the dispersion length of the waveguide, N is the initial soliton number, and $E_{p,\text{fiss}}$ is the pulse energy needed to observe soliton fission (or DWG). At the pulse energy, at which a DW barely emerges in the output spectrum, the fission length equals the fiber length. Thus, if we consider L_{fiss} to be constant (i.e., the fiber length) for each state of the respective DW onset, Eq. (3) shows that a decrease in fission energy indicates an increase in group velocity dispersion β_2 when the system changes from state (A) to state (B). From $L^A_{\text{fiss}} = L^B_{\text{fiss}}$, it follows that $E^A_{p,\text{fiss}}/E^B_{p,\text{fiss}} = |\beta^B_2|/|\beta^A_2|$, if we consider nonlinearity and input pulse width invariant with regard to applied pressure. The relative decrease of the onset energies $E^{\text{atm}}_{p,\text{fiss}}/E^{100\,\text{bar}}_{p,\text{fiss}} = 1.086(\pm 0.041)$ is about 10% when applying 100 bar. The calculated ratio of the group velocity dispersion $|\beta^{100\,\text{bar}}_2|/|\beta^{\text{atm}}_2| = 1.079$ fits well into the error margin of this experimentally determined fission energy ratio.

Note that, in the present case, the fiber geometry was not chosen to obtain the highest possible thermodynamic effect on the mode dispersion (i.e., outside the sensitive domain in Fig. 2). An energy onset of 10% in this thermodynamically silent domain gives reason to expect significant impact of pressure in more optimized fiber designs.

6. FUTURE PROSPECTS

The presented study gives a first glance of the great potential of the thermodynamic tuning of dispersion properties of LiCOFs using straightforward accessible external controls such as temperature or pressure. The large negative TOC of CS_2 and many other solvents [37,38] and their sophisticated nonlinear response enable highly nonlinear devices with unprecedented flexibility and new insights into nonlinear processes. From the fundamental science perspective, temperature tuning as a reconfigurable and easy-to-implement tuning scheme might become a key tool to desirably change the fiber dispersion along the propagation direction to directly observe and to control complex soliton dynamics [45–47]. Promising applications can be envisioned with regard to temperature-induced gratings introducing centimeter-long periodic dispersion changes along the fiber, giving access to multiple soliton break-down processes [47] or quasi-phase-matched modulation instabilities in the normal dispersion regime [48], both observed in glass fibers featuring meter-long periodic changes of the dispersion profile. Also, tuning third-harmonic generation in liquid-core fibers might enable the generation of desired spatial modes in the third-harmonic band [49]. Most notably, longitudinally temperature-induced dispersion tuning represents a unique and reconfigurable approach to implement waveguides with the same functionalities of optical fiber tapers without actually changing the fiber geometry (i.e., "tapering without tapering"). A LiCOF design optimized for a certain laser source can quickly be adapted to another source with different pulse width or emission wavelength by tuning temperature or replacing the core medium.

To demonstrate this potential, we simulate the SCG process in an example CS_2/silica LiCOF design (core diameter: 3.9 μm) in which one mode (TM_{01}) features two ZDWs embracing an interval of anomalous dispersion in the telecom S, C, L-bands as depicted in Fig. 7(a). Such a dispersion design is well known for its capability to spectrally trap solitons and to generate intense Cherenkov radiation to distant wavelengths [50–52]. Launching femtosecond pump pulses with powers easily available from commercial erbium fiber laser systems (here 30 fs, 6 kW, 1560 nm) into this design yields a spectrum featuring two pronounced DWs covering defined spectral intervals. The light generation in this system is highly sensitive to temperature, as the two ZDWs drastically shift within a narrow temperature interval of only 27 K [10°C–37°C, see Fig. 7(a)]. Via the application of a linear temperature gradient along the LiCOF, the phase-matching condition is continuously modified and the DWs spectrally shift accordingly [see Fig. 7(c)]. Additionally, the soliton number steadily increases along the fiber, which enforces a continuous transfer of energy from the soliton trapped in the anomalous dispersion region to the DWs in the normal dispersion region to maintain the

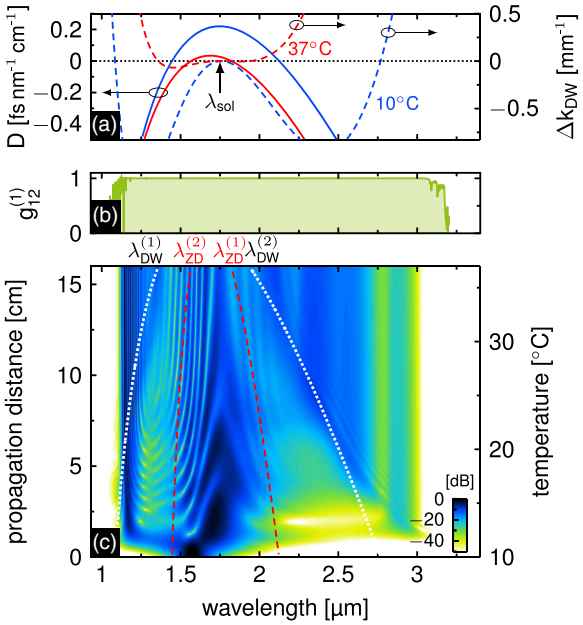

Fig. 7. Gradually shifted double zero-dispersion fiber for highly coherent SCG. (a) Dispersion parameter (left axis) and phase mismatch (right axis) relative to a soliton at 1.75 μm (assumed to be shifted from 1.55 μm), both for two temperatures, (b) first degree of coherence at 16 cm, and (c) the spectral evolution along propagation. A linear slope of the fiber temperature was assumed (see right axis). The lines indicate the shift of the ZDWs λ_{ZD} (red dashed) and the perfectly phase-matched DWs λ_{DW} [white dotted; nonlinear term in Eq. (1) neglected] with temperature.

fundamental soliton condition (i.e., $N = 1$). This drastic energy exhaust of the soliton manifests itself in a smaller impact of the nonlinear phase toward longer propagation distances, which becomes obvious from the improving match between simulated DW locations and calculated Kerr-free phase-matching wavelengths [i.e., $\gamma_s P_s/2 = 0$ in Eq. (1)] in Fig. 7(c) along propagation. As a consequence of the complex dynamics, a broadband soliton-based supercontinuum between 1.2 and 3 μm at 30 dB spectral contrast with high spectral flatness and exceptional pulse-to-pulse coherence [i.e., first degree of correlation [31]; see Fig. 7(b)] is obtained. Recently, it has been shown that such spectra are partly recompressible with standard compression methods and, thus, offer great potential for few-cycle pulse generation [53].

To demonstrate the feasibility of this approach, we conducted further experiments based on an experimental setup comprising an erbium-doped fiber laser (Toptica FemtoFiber Pro, <40 fs, 80 MHz, 1560 nm), a broadband s-waveplate (Altechna, 1550 nm ± 40 nm), and a suitable CS_2/silica LiCOF (core diameter, 3.9 μm; length, 8.5 cm; central heating zone, 3.5 cm). This arrangement is very similar to the one described in Section 3. Here, the s-waveplate was used to generate a radially polarized excitation beam to excite a TM_{01} fiber mode and was aligned directly in front of the fiber coupling stage to avoid perturbations by mirrors. By using silica aspheric lenses, comparably clean TM_{01} mode field distributions with coupling efficiencies of 25% were achieved at the liquid-core fiber output (see upper left mode image in Fig. 8). The input and output modes were imaged with a cooled InGaAs camera (ABS Jena IK1513) or a phosphorized CMOS camera (DataRay WinCamD-IR), while the radial output polarization was checked by rotating an analyzer inserted between output lens and camera. The output light was guided to a near-IR OSA or an FTIR spectrometer (Thorlabs OSA305) using an InF_3 fiber. The liquid-core fiber was heated in its central part with a Peltier element placed between the two OFMs [similar to the arrangement shown in Fig. 3(d)].

The colored curves in Fig. 8 show example output spectra for four different temperatures, which are homogeneously applied

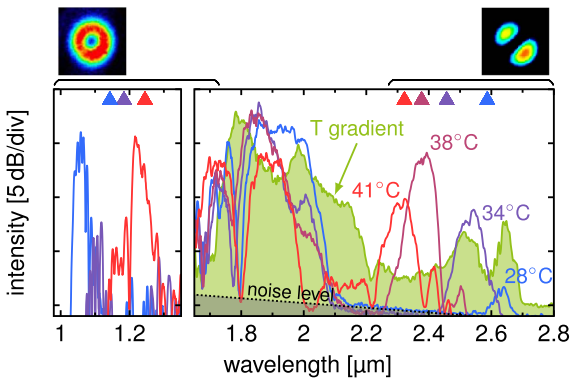

Fig. 8. Measured output spectra of a liquid-core fiber (core, CS_2; cladding, silica; core diameter, 3.9 μm) pumped by a TM_{01}-like mode (0.31 nJ pulse energy) at four different temperatures (colored curves). The triangles mark the calculated location of the phase-matched DWs considering a soliton at 1.75 μm, 21.2 kW peak power, and a fiber with 3.95 μm core diameter. The green spectrum in the background refers to a non-optimized temperature gradient mentioned in the main text. The black bars above the diagram indicate the spectral intervals of the filters used for obtaining the mode images on top of the plot.

across the heating zone. Distinct DWs appear on both sides of the pump regime at 1.56 μm (latter not shown in the figure to highlight the DW behavior) and shift considerably in wavelength toward the pump regime when increasing the temperature by only 13 K, which is more than 200 nm on the long-wave and more than 150 nm on the short-wave side. This wavelength shift correlates well to the calculated phase-matching wavelengths based on Eq. (1) (see triangular marks in Fig. 8) under assumption of a soliton wavelength of 1.75 μm with 21.2 kW peak power ($N = 4.1$), and a nonlinear gain γ_s of 53 W^{-1} km^{-1}. Smallest deviations in pulse shape and chirp, temperature profile, and core diameter of the fiber have a strong impact in this critical dispersion landscape and might explain the slightly smaller shift of the predicted DW location. The limited dynamic range of the FTIR spectrometer did not allow observation of the long-wave DW at even lower temperatures.

The intensity pattern of the output mode shows the characteristic doughnut-like shape of a TM_{01} mode at short wavelength. On the red side of the pump pulse, however, the intensity pattern carries the characteristics of a LP_{11} mode, which might be caused by coupling between the TM_{01} and HE_{21} modes due to the reduced difference in effective mode index toward longer wavelengths, which might be additionally facilitated by nonlinear perturbations. A full mode analysis and a detailed study of the complex nonlinear broadening process will be published in a separate work.

In addition to the constant temperature experiments, we implemented a temperature gradient using the thermal radiation from a hot spot (heating element with thickness 1 mm at approx. 45°C) attached to the fiber in front of the OFM on the output side. The output spectrum (green filled area in Fig. 8) reveals a more homogeneous distribution of the generated frequencies between the soliton domain (i.e., around 1.8 μm) and the long-wave DW. Even though the shape of the temperature gradient is to some extent uncontrolled and quantitatively different to that presented in Fig. 7, these results qualitatively confirm the operation principle of the device discussed in Fig. 7. This comparably simple design, which in fact allows to change the waveguide properties within milliseconds, highlights the big opportunities of externally controllable LiCOFs and allows for further straightforward improvements via, e.g., modifying ZDW trajectories and pump conditions.

In addition to dispersion management, thermodynamic tuning also allows to alter the nonlinear response of the core material itself and thus the dynamic response of the entire nonlinear waveguide. For instance, the pressure and temperature effect on the highly noninstantaneous nonlinearity of CS_2 is quite dominant [54]. Gaining active control over the temporal behavior of the nonlinearity of solvents like CS_2 is an interesting unique approach, which might help to understand novel soliton dynamics in a hybrid type of nonlinear regime, which we just started to understand [32], and to overcome the bandwidth limits dictated by this novel dynamics.

7. CONCLUSION

Manipulating nonlinear optical processes via tuning the properties of an underlying nonlinear waveguide represents a key concept to understand the ongoing physical processes, to reach previously inaccessible spectral domains and functionalities, and to adapt light generation to specified applications. In this

contribution, we reported on the experimental demonstration of tuning the soliton fission process at the onset of SCG via changing the thermodynamic properties of liquid-core fibers. We showed that tuning the temperature enables modification of the mode dispersion, directly affecting the phase-matching condition of soliton-mediated DWG and, thus, allowing for external control of nonlinear processes in real time.

The investigated fiber system, optimized for soliton fission and high temperature sensitivity, consists of a carbon disulfide core of diameter of 3.3 μm and a silica cladding pumped by a 350 fs thulium fiber laser operating at 1.92 μm. Efficient DWG was observed at pulse energies below 0.5 nJ and peak powers around 1 kW. In accordance with simulations and phase-matching considerations, which include a novel temperature- and pressure-dependent material dispersion model of CS_2, we observed that tuning the temperature of a well-selected part of the LiCOF by only 30 K leads to a linear redshift of the emitted DW by more than 100 nm and a decrease of the soliton fission onset energy. The observed spectral behavior can be directly linked to a modification of the underlying phase-matching condition, allowing us to tune the emission wavelength to a high degree. The low boiling point of CS_2 (46°C) might suggest a limited temperature tuning range, but the low freezing point of this solvent (−112°C) gives plenty of room to even triple the tuning range demonstrated here considering efficient cooling schemes. Moreover, there are many other highly transparent liquids with boiling points well above 100°C and similarly strong thermo-optical coefficients [37,38] that need to be explored more in future studies.

Additionally, we found a decrease of the soliton fission onset energy when external pressure is applied due to the increase of the group velocity dispersion of the fiber as a result of the piezo-optical effect (i.e., the application of 100 bar of static pressure), which is counterintuitive due to the often assumed incompressibility of liquids. Despite the weak impact of the piezo-optical effect and the challenges of high-pressure experiments, the impact of pressure can become dominant, e.g., in the case of sealed liquid-core devices [38], and should be considered an additional thermodynamic degree of freedom.

Finally, we discussed the potential of liquid-core optical fibers with regard to tunable nonlinear light generation in general and demonstrated it with a simulation based on a design with gradually changing temperature. The resulting shift in the ZDWs leads to the generation of a nearly two-octave-spanning supercontinuum between 1.2 and 3 μm with high spectral flatness and a perfect pulse-to-pulse spectral coherence at comparably long input pulse durations. To verify the feasibility and the impact of a gradually changing dispersion profile experimentally, we have investigated higher order mode soliton-based SCG in a liquid-core fiber, which revealed a temperature-induced shift of DWs at short and long wavelengths over hundreds of nanometers within only 13 K of temperature change. Additionally, we observed spectral flattening, i.e., a more even distribution of frequencies, that is solely imposed by an unspecified temperature gradient and, thus, qualitatively supports the simulations discussed above.

We are convinced that, in particular, temperature treatment in LiCOFs will play a similarly important role as pressure tuning in gas-filled hollow core fibers, but with a higher degree of flexibility, as it facilitates, e.g., external control over sophisticated dispersion landscapes (and potentially nonlinearity) at similarly large signal detunings. Harvesting the full thermodynamic features of liquids promises new insights into nonlinear optical processes (e.g., to observe new solitary states or to understand molecular dynamics) and highly tunable light sources for applications including single-shot spectroscopy, medical imaging, or metrology.

Funding. Deutsche Forschungsgemeinschaft (DFG) (SCHM2655/3-1, IRTG 2101); European Social Fund (ESF) (2015-0021, 2015FGI0011); European Regional Development Fund (ERDF); University of Central Florida (UCF) (Project "Fundamental Fiber Laser Science for High Powers" 321095).

Acknowledgment. Fabian Stutzki acknowledges support by the Carl-Zeiss-Stiftung. Martin Gebhardt acknowledges support by the Helmholtz-Institute Jena.

See Supplement 1 for supporting content.

REFERENCES

1. T. Gottschall, T. Meyer, M. Baumgartl, C. Jauregui, M. Schmitt, J. Popp, J. Limpert, and A. Tünnermann, "Fiber-based light sources for biomedical applications of coherent anti-Stokes Raman scattering microscopy," Laser Photon. Rev. **9**, 435–451 (2015).
2. C. Kaminski, R. Watt, A. Elder, J. Frank, and J. Hult, "Supercontinuum radiation for applications in chemical sensing and microscopy," Appl. Phys. B **92**, 367–378 (2008).
3. J. M. Langridge, T. Laurila, R. S. Watt, R. L. Jones, C. F. Kaminski, and J. Hult, "Cavity enhanced absorption spectroscopy of multiple trace gas species using a supercontinuum radiation source," Opt. Express **16**, 10178–10188 (2008).
4. A. G. Griffith, R. K. Lau, J. Cardenas, Y. Okawachi, A. Mohanty, R. Fain, Y. H. D. Lee, M. Yu, C. T. Phare, C. B. Poitras, A. L. Gaeta, and M. Lipson, "Silicon-chip mid-infrared frequency comb generation," Nat. Commun. **6**, 7299 (2015).
5. T. Udem, R. Holzwarth, and T. W. Hänsch, "Optical frequency metrology," Nature **416**, 233–237 (2002).
6. R. Slavík, F. Parmigiani, J. Kakande, C. Lundström, M. Sjödin, P. A. Andrekson, R. Weerasuriya, S. Sygletos, A. D. Ellis, L. Grüner-Nielsen, D. Jakobsen, S. Herstrøm, R. Phelan, J. O'Gorman, A. Bogris, D. Syvridis, S. Dasgupta, P. Petropoulos, and D. J. Richardson, "All-optical phase and amplitude regenerator for next-generation telecommunications systems," Nat. Photonics **4**, 690–695 (2010).
7. J. Pfeifle, V. Brasch, M. Lauermann, Y. Yu, D. Wegner, T. Herr, K. Hartinger, P. Schindler, J. Li, D. Hillerkuss, R. Schmogrow, C. Weimann, R. Holzwarth, W. Freude, J. Leuthold, T. J. Kippenberg, and C. Koos, "Coherent terabit communications with microresonator Kerr frequency combs," Nat. Photonics **8**, 375–380 (2014).
8. E. Lucas, H. Guo, J. D. Jost, M. Karpov, and T. J. Kippenberg, "Detuning-dependent properties and dispersion-induced instabilities of temporal dissipative Kerr solitons in optical microresonators," Phys. Rev. A **95**, 043822 (2017).
9. Y. Tang, L. G. Wright, K. Charan, T. Wang, C. Xu, and F. W. Wise, "Generation of intense 100 fs solitons tunable from 2 to 4.3 μm in fluoride fiber," Optica **3**, 948–951 (2016).
10. M. Chemnitz, M. Baumgartl, T. Meyer, C. Jauregui, B. Dietzek, J. Popp, J. Limpert, and A. Tünnermann, "Widely tuneable fiber optical parametric amplifier for coherent anti-Stokes Raman scattering microscopy," Opt. Express **20**, 26583–26595 (2012).
11. T. Elsmann, A. Lorenz, N. S. Yazd, T. Habisreuther, J. Dellith, A. Schwuchow, J. Bierlich, K. Schuster, M. Rothhardt, L. Kido, and H. Bartelt, "High temperature sensing with fiber Bragg gratings in sapphire-derived all-glass optical fibers," Opt. Express **22**, 26825–26833 (2014).
12. C. Joshi, J. K. Jang, K. Luke, X. Ji, S. A. Miller, A. Klenner, Y. Okawachi, M. Lipson, and A. L. Gaeta, "Thermally controlled comb generation and soliton modelocking in microresonators," Opt. Lett. **41**, 2565–2568 (2016).

13. G. Ghosh, "Model for the thermo-optic coefficients of some standard optical glasses," J. Non-Cryst. Solids **189**, 191–196 (1995).
14. P. St. J. Russell, P. Hölzer, W. Chang, A. Abdolvand, and J. C. Travers, "Hollow-core photonic crystal fibres for gas-based nonlinear optics," Nat. Photonics **8**, 278–286 (2014).
15. S. Kedenburg, M. Vieweg, T. Gissibl, and H. Giessen, "Linear refractive index and absorption measurements of nonlinear optical liquids in the visible and near-infrared spectral region," Opt. Mater. Express **2**, 1588–1611 (2012).
16. R. W. Boyd and G. L. Fischer, *Nonlinear Optical Materials* (Elsevier, 2001).
17. H. W. Lee, M. A. Schmidt, P. Uebel, H. Tyagi, N. Y. Joly, M. Scharrer, and P. St. J. Russell, "Optofluidic refractive-index sensor in step-index fiber with parallel hollow micro-channel," Opt. Express **19**, 8200–8207 (2011).
18. Y. Xu, X. Chen, and Y. Zhu, "High sensitive temperature sensor using a liquid-core optical fiber with small refractive index difference between core and cladding materials," Sensors **8**, 1872–1878 (2008).
19. Z. Li and D. Psaltis, "Optofluidic dye lasers," Microfluid. Nanofluid. **4**, 145–158 (2008).
20. X. Fan and S.-H. Yun, "The potential of optofluidic biolasers," Nat. Methods **11**, 141–147 (2014).
21. R. M. Gerosa, A. Sudirman, L. D. S. Menezes, W. Margulis, and C. J. S. de Matos, "All-fiber high repetition rate microfluidic dye laser," Optica **2**, 186–193 (2015).
22. M. Vieweg, S. Pricking, T. Gissibl, Y. Kartashov, L. Torner, and H. Giessen, "Tunable ultrafast nonlinear optofluidic coupler," Opt. Lett. **37**, 1058–1060 (2012).
23. B. Kuhlmey, B. Eggleton, and D. Wu, "Fluid-filled solid-core photonic bandgap fibers," J. Lightwave Technol. **27**, 1617–1630 (2009).
24. P. Mach, M. Dolinski, K. W. Baldwin, J. A. Rogers, C. Kerbage, R. S. Windeler, and B. J. Eggleton, "Tunable microfluidic optical fiber," Appl. Phys. Lett. **80**, 4294–4296 (2002).
25. Y. Liu, Y. Wang, B. Sun, C. Liao, J. Song, K. Yang, G. Wang, Q. Wang, G. Yin, and J. Zhou, "Compact tunable multibandpass filters based on liquid-filled photonic crystal fibers," Opt. Lett. **39**, 2148–2151 (2014).
26. L. Velázquez-Ibarra, A. Díez, E. Silvestre, and M. V. Andrés, "Wideband tuning of four-wave mixing in solid-core liquid-filled photonic crystal fibers," Opt. Lett. **41**, 2600–2603 (2016).
27. Y. Peng, J. Hou, Y. Zhang, Z. Huang, R. Xiao, and Q. Lu, "Temperature sensing using the bandgap-like effect in a selectively liquid-filled photonic crystal fiber," Opt. Lett. **38**, 263–265 (2013).
28. T. Gissibl, M. Vieweg, M. M. Vogel, M. Aboud Ahmed, T. Graf, and H. Giessen, "Preparation and characterization of a large mode area liquid-filled photonic crystal fiber: transition from isolated to coupled spatial modes," Appl. Phys. B **106**, 521–527 (2012).
29. D. V. Skryabin and A. V. Gorbach, "Colloquium: Looking at a soliton through the prism of optical supercontinuum," Rev. Mod. Phys. **82**, 1287–1299 (2010).
30. N. Akhmediev and M. Karlsson, "Cherenkov radiation emitted by solitons in optical fibers," Phys. Rev. A **51**, 2602–2607 (1995).
31. J. M. Dudley, G. Genty, and S. Coen, "Supercontinuum generation in photonic crystal fiber," Rev. Mod. Phys. **78**, 1135–1184 (2006).
32. M. Chemnitz, M. Gebhardt, C. Gaida, F. Stutzki, J. Kobelke, J. Limpert, A. Tünnermann, and M. A. Schmidt, "Hybrid soliton dynamics in liquid-core fibres," Nat. Commun. **8**, 42 (2017).
33. M. Reichert, H. Hu, M. R. Ferdinandus, M. Seidel, P. Zhao, T. R. Ensley, D. Peceli, J. M. Reed, D. A. Fishman, S. Webster, D. J. Hagan, and E. W. Van Stryland, "Temporal, spectral, and polarization dependence of the nonlinear optical response of carbon disulfide," Optica **1**, 436–445 (2014).
34. E. Reisler, H. Eisenberg, and A. P. Minton, "Temperature and density dependence of the refractive index of pure liquids," J. Chem. Soc. Faraday Trans. 2 **68**, 1001–1015 (1972).
35. C. D. Keefe and S. Mac Innis, "Temperature dependence of the optical properties of liquid toluene between 4000 and 400 cm^{-1} from 30 to 105°C," J. Mol. Struct. **737**, 207–219 (2005).
36. H. El-Kashef, "Study of the refractive properties of laser dye solvents: toluene, carbon disulphide, chloroform, and benzene," Opt. Mater. **20**, 81–86 (2002).
37. K. Moutzouris, M. Papamichael, S. C. Betsis, I. Stavrakas, G. Hloupis, and D. Triantis, "Refractive, dispersive and thermo-optic properties of twelve organic solvents in the visible and near-infrared," Appl. Phys. B **116**, 617–622 (2013).
38. S. Pumpe, M. Chemnitz, J. Kobelke, and M. A. Schmidt, "Monolithic optofluidic mode coupler for broadband thermo- and piezo-optical characterization of liquids," Opt. Express **25**, 22932–22946 (2017).
39. J. Matsuoka, N. Kitamura, S. Fujinaga, T. Kitaoka, and H. Tamashita, "Temperature dependence of refractive index of SiO_2 glass," J. Non-Cryst. Solids **135**, 86–89 (1991).
40. W. J. Tropf, "Temperature-dependent refractive index models for BaF_2, CaF_2, MgF_2, SrF_2, LiF, NaF, KCl, ZnS, and ZnSe," Opt. Eng. **34**, 1369–1373 (1995).
41. D. J. Coumou, E. L. Mackor, and J. Hijmans, "Isotropic light-scattering in pure liquids," Trans. Faraday Soc. **60**, 1539–1547 (1964).
42. J. W. Fleming, "Dispersion in GeO_2–SiO_2 glasses," Appl. Opt. **23**, 4486–4493 (1984).
43. M. Chemnitz, C. Gaida, M. Gebhardt, F. Stutzki, J. Kobelke, A. Tünnermann, J. Limpert, and M. A. Schmidt, "Carbon chloride-core fibers for soliton mediated supercontinuum generation," Opt. Express **26**, 3221–3235 (2018).
44. J. N. Elgin, T. Brabec, and S. M. Kelly, "A perturbative theory of soliton propagation in the presence of third order dispersion," Opt. Commun. **114**, 321–328 (1995).
45. C. Conti, M. A. Schmidt, P. St. J. Russell, and F. Biancalana, "Highly noninstantaneous solitons in liquid-core photonic crystal fibers," Phys. Rev. Lett. **105**, 263902 (2010).
46. A. V. Gorbach and D. V. Skryabin, "Light trapping in gravity-like potentials and expansion of supercontinuum spectra in photonic-crystal fibres," Nat. Photonics **1**, 653–657 (2007).
47. A. Bendahmane, F. Braud, and M. Conforti, "Dynamics of cascaded resonant radiations in a dispersion-varying optical fiber," Optica **1**, 243–249 (2014).
48. A. Mussot, M. Conforti, S. Trillo, F. Copie, and A. Kudlinski, "Modulation instability in dispersion oscillating fibers," Adv. Opt. Photon. **10**, 1–42 (2018).
49. S. C. Warren-Smith, J. Wie, M. Chemnitz, R. Kostecki, H. Ebendorff-Heidepriem, T. M. Monro, and M. A. Schmidt, "Third harmonic generation in exposed-core microstructured optical fibers," Opt. Express **24**, 17860–17867 (2016).
50. N. Granzow, M. A. Schmidt, W. Chang, L. Wang, Q. Coulombier, J. Troles, P. Toupin, I. Hartl, K. F. Lee, M. E. Fermann, L. Wondraczek, and P. St. J. Russell, "Mid-infrared supercontinuum generation in As_2S_3-silica 'nano-spike' step-index waveguide," Opt. Express **21**, 10969–10977 (2013).
51. R. K. W. Lau, M. R. E. Lamont, A. G. Griffith, Y. Okawachi, M. Lipson, and A. L. Gaeta, "Octave-spanning mid-infrared supercontinuum generation in silicon nanowaveguides," Opt. Lett. **39**, 4518–4521 (2014).
52. V. Brasch, T. Herr, M. Geiselmann, G. Lihachev, M. H. P. Pfeiffer, M. L. Gorodetsky, and T. J. Kippenberg, "Photonic chip-based optical frequency comb using soliton Cherenkov radiation," Science **351**, 357–360 (2016).
53. I. Babushkin, A. Tajalli, H. Sayinc, U. Morgner, G. Steinmeyer, and A. Demircan, "Simple route toward efficient frequency conversion for generation of fully coherent supercontinua in the mid-IR and UV range," Light Sci. Appl. **6**, e16218 (2016).
54. A. Idrissi, M. Ricci, P. Bartolini, and R. Righini, "Optical Kerr-effect investigation of the reorientational dynamics of CS_2 in CCl_4 solutions," J. Chem. Phys. **111**, 4148–4152 (1999).